Optics and Lasers in Engineering 86 (2016) 83–91

Contents lists available at ScienceDirect

Optics and Lasers in Engineering

journal homepage: www.elsevier.com/locate/optlaseng

Structure light telecentric stereoscopic vision 3D measurement system based on Scheimpflug condition

Qing Mei [a], Jian Gao [a,b,*], Hui Lin [a,c], Yun Chen [a,b], He Yunbo [a,**], Wei Wang [a], Guanjin Zhang [a], Xin Chen [a,b]

[a] Key Laboratory of Mechanical Equipment Manufacturing and Control Technology of Ministry of Education, School of Electromechanical Engineering, Guangdong University of Technology, Guangzhou 510006, China
[b] Guangdong Provincial Key Laboratory of Computer Integrated Manufacturing, School of Electromechanical Engineering, Guangdong University of Technology, Guangzhou 510006, China
[c] School of Physics and Mechatronics Engineering, Shaoguan University, Shaoguan 512005, China

ARTICLE INFO

Article history:
Received 27 January 2016
Received in revised form
25 May 2016
Accepted 25 May 2016

Keywords:
Scheimpflug condition
Structure light
Telecentric stereoscopic vision
Wafer
3D Reconstruction

ABSTRACT

We designed a new three-dimensional (3D) measurement system for micro components: a structure light telecentric stereoscopic vision 3D measurement system based on the Scheimpflug condition. This system creatively combines the telecentric imaging model and the Scheimpflug condition on the basis of structure light stereoscopic vision, having benefits of a wide measurement range, high accuracy, fast speed, and low price. The system measurement range is 20 mm × 13 mm × 6 mm, the lateral resolution is 20 μm, and the practical vertical resolution reaches 2.6 μm, which is close to the theoretical value of 2 μm and well satisfies the 3D measurement needs of micro components such as semiconductor devices, photoelectron elements, and micro-electromechanical systems. In this paper, we first introduce the principle and structure of the system and then present the system calibration and 3D reconstruction. We then present an experiment that was performed for the 3D reconstruction of the surface topography of a wafer, followed by a discussion. Finally, the conclusions are presented.

1. Introduction

With the rapid development of microelectronic technology, all kinds of microelements, such semiconductor devices, photoelectron elements, and micro-electromechanical systems (MEMS), are mass-produced in industry and applied in various high-end electronics and precise instruments, which brings a new challenge to modern detection methods. The traditional contact-detection method, for example, Micro-CMM [1,2] has not satisfied the requirements of fast, highly accurate, and non-destructive detection in the microelectronics manufacturing industry. Therefore, many scholars—both domestic and foreign—have proposed non-contact optical measurement methods, such as confocal microscopy [3,4], white-light interferometry [5,6], and microscopic fringe projection [7–10]. Even if the resolution of confocal microscopy and white-light interferometry reach nano-level, the measurement range is merely several millimeters. Moreover, both confocal microscopy and white-light interferometry involve complex structures with very precise optical and the piezoelectric ceramic driving systems, which are expensive and difficult to realize. Microscopic fringe projection draws attention for its high profile sampling density, high resolution, easiness to realize, and low price. In traditional microscopic fringe projection, a stereoscopic microscope is employed as basic optical system with an LCOS/DLP projector and a CCD camera installed on the two cylinders of the stereoscopic microscope, i.e., the projection-end and imaging-end, respectively. However, the depth of focus of a stereoscopic microscope is relatively small under common conditions; thus, the entire three-dimensional (3D) shape of the object cannot be measured at one time. Compared with an ordinary lens, a telecentric lens has the characteristics of a low distortion, magnification constancy, a high depth of focus, and a good image resolution [11] because its light path is an orthographic projection [12,13]. For this reason, researchers have proposed telecentric fringe projection profilometry [14], which replaces the lenses of the DLP micro projector and CCD camera with telecentric lenses on the basis of the triangulation principle. However, the telecentric lenses must be tilted in accordance with the triangulation principle; thus, they must have a

* Corresponding author at: Key Laboratory of Mechanical Equipment Manufacturing and Control Technology of Ministry of Education, School of Electromechanical Engineering, Guangdong University of Technology, Guangzhou 510006, China.
** Corresponding author.
E-mail addresses: gaojian@gdut.edu.cn (J. Gao), heyunbo@gdut.edu.cn (H. Yunbo).

http://dx.doi.org/10.1016/j.optlaseng.2016.05.021
0143-8166/

high depth of focus to ensure that the camera captures a clear image in the whole field of view. Nonetheless, for telecentric lenses, a high depth of focus causes the aperture to become smaller, which reduces the resolution, resulting in a lower resolution of the measurement system on the Z axis (vertical resolution). As a fact, theoretically, the vertical resolution of the measurement system based on this fringe projection is about one order of magnitude better than the lateral resolution (the resolution of the lens) [15].

To consider both the depth of focus and resolution, we improved the structure of telecentric fringe projection profilometry and designed a new 3D measurement system for micro components: a structure light telecentric stereoscopic vision 3D measurement system based on the Scheimpflug condition [16]. Recently, Xiang Peng et al. researched the calibration of the Scheimpflug telecentric lens. Interestingly, the inclination of the sensor was considered as additional distortion, which differed from reality [17]. In the Scheimpflug condition, the depth of focus can be enlarged greatly without decreasing the resolution of the lens, which ensures that the measurement system has a good resolution over a wider measurement range. The system measurement range is 20 mm × 13 mm × 6 mm, the lateral resolution is 20 μm, and the practical vertical resolution reaches 2. 6 μm, which is close to the theoretical vertical resolution of 2 μm, well satisfying the 3D measurement needs of micro components such as semiconductor devices, photoelectron elements, and MEMS.

In Section 2, we describe the principle and structure of structure light telecentric stereoscopic vision based on the Scheimpflug condition. In Section 3, we describe the system calibration. In Section 4, we describe the 3D reconstruction. In Section 5, we detail an experiment and present a discussion. A conclusion is drawn in Section 6.

2. Principle and structure

2.1. Telecentric imaging model

The imaging model of a telecentric lens is orthographic projection, which differs significantly from the imaging model of an ordinary lens, i.e., perspective projection. Because image-side telecentric lenses are rarely used in real applications and are not used in the measurement system described herein, we introduce only bilateral and object-side telecentric lenses. Figs. 1 and 2 show the light paths of bilateral and object-side telecentric lenses, respectively. As for bilateral telecentric lenses, both the light rays from the object and the image side are parallel to the optical axis, and both the projection centers on the object and the image side are located at infinity. Within certain limits, changing the object or the image distance has no effect on the magnification of the lens. In Fig. 1, the magnification of the bilateral lens is $m_1=f_2/f_1$. With regard to the object telecentric lens, there are only the light rays from object side parallel to the optical axis; the light rays from the image side intersect at the focus point, where the aperture stop is located. Only the projection center on the object side is located at infinity. Within a certain range, changing the object distance does not affect the magnification of the lens. In Fig. 2, the magnification of the object-side telecentric lens is $m_2=(b-f)/f$. This magnification constancy characteristic of bilateral and object-side telecentric lenses makes them suitable for precise measurement, which differs significantly from the pinhole model of ordinary lenses.

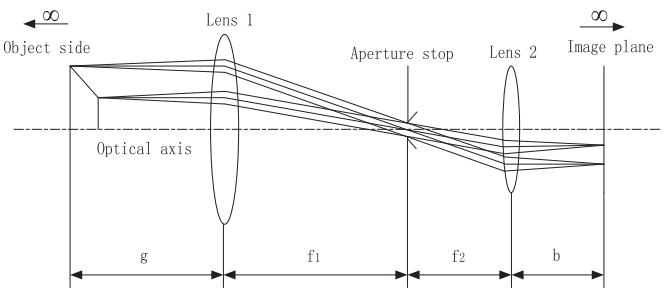

Fig. 1. Model of bi-telecentric light path.

2.2. Scheimpflug condition

As shown in Fig. 3, in a common optical system, the lens plane (LP) and image plane (IP) are parallel, and the plane of focus (PoF) is parallel to the lens and image planes. The object plane intersects with the PoF only at a line when it is not parallel to LP or IP. In this way, only a small region of the object is located in the focus range, and other regions remain in a defocusing state; thus, only a part of the image is clear, and other parts are blurred. However, under the Scheimpflug condition, the lens plane is installed at a certain angle relative to the CCD chip plane, which makes the PoF intersect with the lens plane and image plane at the same line. As shown in Fig. 4, when the object plane coincides with the PoF, the camera is in a pure focusing state, and the depth of focus becomes wedge-shaped and enlarged. In Fig. 5, the imaging quality is compared between the common optical system and the optical system in the Scheimpflug condition. It is obvious that the image quality of the optical system in the Scheimpflug condition is clearly far better than that of the common optical system.

2.3. Principle and structure design of the measurement system proposed

As shown in Fig. 6, via a connecting cylinder, an object-side telecentric lens is installed in front of the DMD chip (0. 45″) of the DLP projector, whose original lens is removed, and a bi-telecentric lens with the Scheimpflug adjustment [18] (TCSM036, OPTO

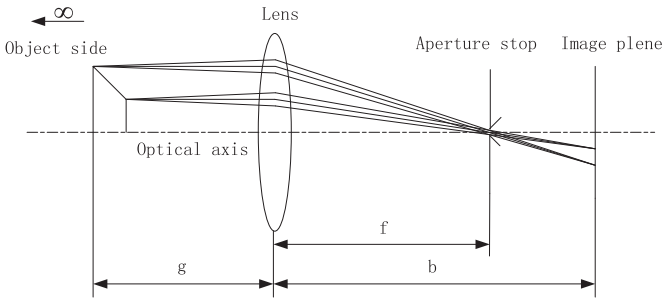

Fig. 2. Model of object-side telecentric light path.

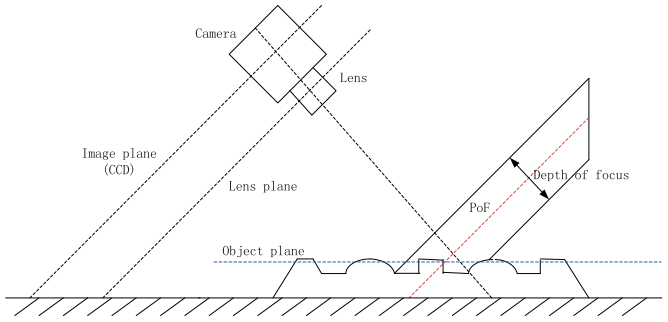

Fig. 3. Schematic diagram of common optical system.

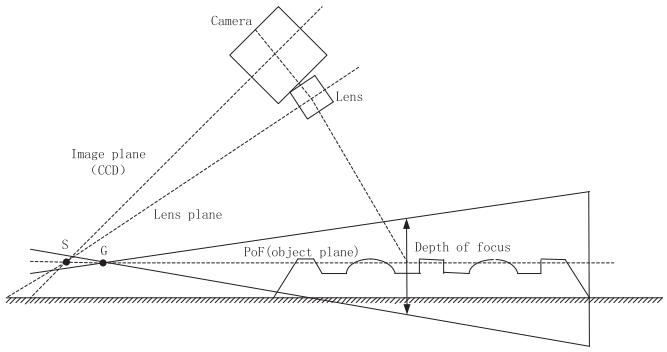

Fig. 4. Schematic diagram of the optical system on Scheimpflug condition.

Corporation) is installed on a CCD camera with a chip size of 1/1. 8′. The magnification of the object side and the bilateral telecentric lens are 0.5 and 0.243, respectively. Fig. 7 shows the measurement system constructed in our laboratory. Using the Scheimpflug adjustment, the lens plane can be tilted at a certain angle relative to the CCD chip plane. In the Scheimpflug condition, the relation between the angles θ and Φ satisfies $\tan\theta = m\tan\Phi$, where θ is the angle between the lens plane and the CCD chip plane, Φ is the angle between the lens plane and the object plane, and m is the magnification of the camera lens. The value of Φ is set according to θ, and the work distance is regulated on the basis of the lens parametre, such that the Scheimpflug condition is satisfied.

When implementing the actual measurement, the structured fringe pattern generated by the computer is projected vertically onto the object by the modified DLP projector. The structured fringe pattern is deformed by the modulation of the object height. Then, the telecentric camera in the Scheimpflug condition captures the deformed fringe images and sends them back the computer. A software program computes the absolute phase of every pixel point on the structured fringe image, matches the pixels between the CCD plane of the camera and the DMD plane of the DLP projector, and finally computes the coordinate (X_w, Y_w, Z_w) of a point in space by the structure light triangulation method according to the system parametres, which are calibrated in advance. To compute the absolute phase of every pixel point, the well-known gray code-combined phase-shift algorithm [19] is employed in this paper. According to the four-step phase-shift algorithm,

$$I_n(x, y)=I'(x, y)+I''(x, y)\cos[\varphi(x, y)+n\bullet\pi/2] \quad (1)$$

where n=0, 1, 2, 3; x, y are the pixel indices; $I_n(x, y)$ is the intensity of the nth phase-shifted image; $I'(x, y)$ is the average intensity; $I''(x, y)$ is the modulation intensity; and $\varphi(x, y)$ is the phase map of the fringe pattern. We obtained

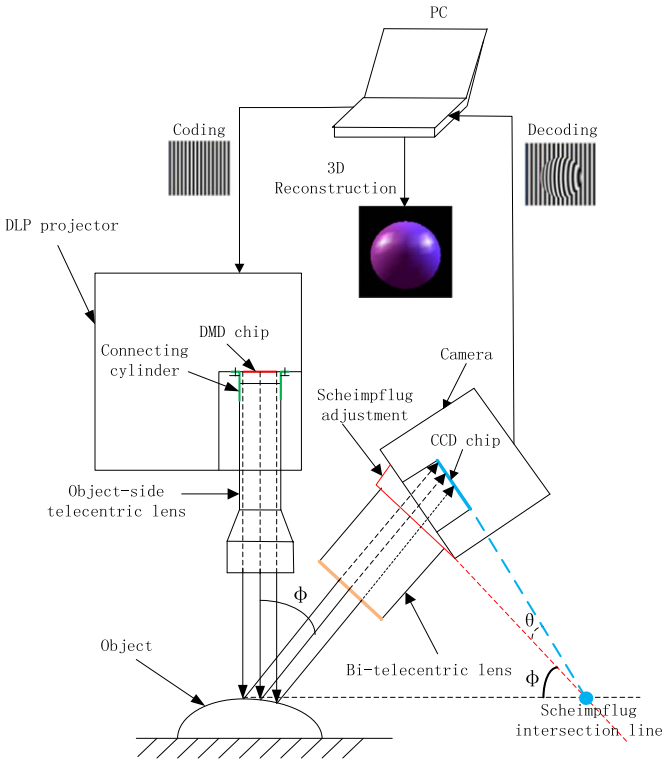

Fig. 6. Global structure figure of the measurement system.

Fig. 7. The measurement system constructed in our laboratory.

$$\varphi(x, y)=\arctan\frac{I_4(x, y)-I_2(x, y)}{I_1(x, y)-I_3(x, y)} \quad (2)$$

where $\varphi(x, y)$ is the discontinuous wrapped phase, whose value

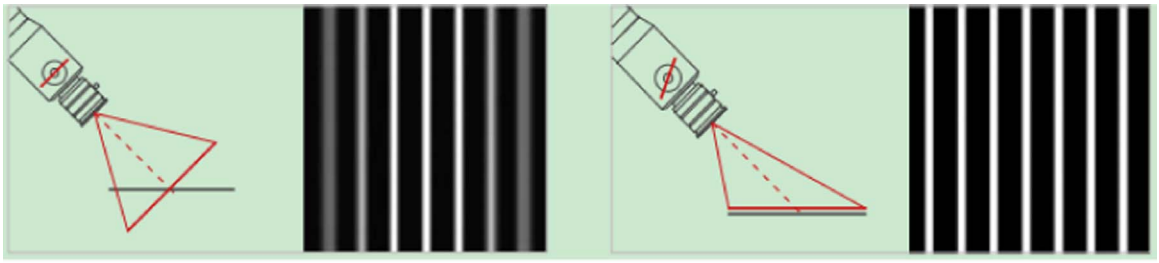

Fig. 5. Comparison on the imaging quality between two kinds of optical system.

domain is $-\pi \le \varphi(x, y) \le \pi$. To obtain the absolute phase $\Phi(x, y)$ over the whole field of view, a phase-unwrapping process must be implemented on $\varphi(x, y)$. The relationship between $\Phi(x, y)$ and $\varphi(x, y)$ can be described as

$$\Phi(x, y)=\varphi(x, y)+2k\pi \tag{3}$$

where k is an integer denoting the fringe order. Through the gray code combined phase-shift algorithm, k can be solved by gray coding and decoding, which is detailed in [19].

3. System calibration

3.1. Calibration of telecentric camera on Scheimpflug condition

Combining the Scheimpflug condition and the telecentric light path model, the imaging model of the telecentric camera in Scheimpflug condition is obtained, as shown in Fig. 8. The telecentric camera in the Scheimpflug condition, undergoes the process below to transform a point $P^w(X_w, Y_w, Z_w)$ of the world coordinate system (WCS) in space into the corresponding pixel point $Q^c(u^c, v^c)$ of the camera pixel coordinate system (PCS). First, the coordinates $P^w(X_w, Y_w, Z_w)$ of a point in space in the WCS are transformed into the coordinates $P^c(X_c, Y_c, Z_c)$ in the camera coordinate system (CCS). Then, $P^c(X_c, Y_c, Z_c)$ is projected onto the virtual parallel image plane, i.e., converted to the two-dimensional point $Q'(u', v')$. Next, the lens distortion is applied to $Q'(u', v')$, transforming it into the distorted point $\tilde{Q}'(\tilde{u}', \tilde{v}')$. After that, the point $\tilde{Q}'(\tilde{u}', \tilde{v}')$ is projected to the point $Q^t(u^t, v^t)$ on the tilt image plane, remaining in metric coordinates. Finally, the point $Q^t(u^t, v^t)$ is transformed into the pixel point $Q^c(u^c, v^c)$ in the PCS of the camera. The aforementioned process can be written as follows:

$$P^w \longrightarrow P^c \longrightarrow Q' \longrightarrow \tilde{Q}' \longrightarrow Q^t \longrightarrow Q^c$$

Through the transformation process from the point $P^w(X_w, Y_w, Z_w)$ in the WCS to the pixel point $Q^c(u^c, v^c)$ in the PCS of the camera, the mapping equation from P^w to Q^c can be written as

$$\begin{bmatrix} u^c \\ v^c \\ 1 \end{bmatrix} = T_{3\times3} \begin{bmatrix} m^c/du^c & 0 & u_0^c \\ 0 & m^c/dv^c & v_0^c \\ 0 & 0 & 1 \end{bmatrix} \begin{bmatrix} r_{11} & r_{12} & r_{13} t_x^c \\ r_{21} & r_{22} & r_{23} t_y^c \\ 0 & 0 & 0 \quad 1 \end{bmatrix} \begin{bmatrix} X_w \\ Y_w \\ Z_w \\ 1 \end{bmatrix} \tag{4}$$

where $T_{3\times3}$ is the matrix constituted by the two Scheimpflug tilt angles ρ and τ, which can be written as

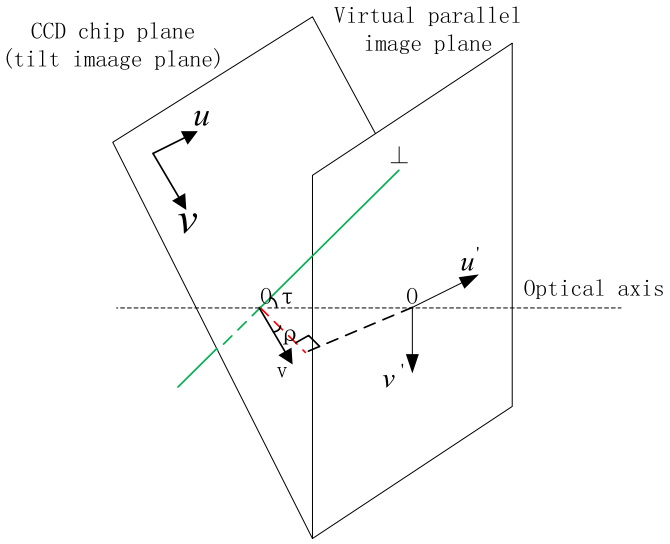

Fig. 9. Schematic diagram of Scheimpflug angle.

Table 1
The inner and external parametres of telecentric camera on Scheimpflug condition.

Parametre	$\rho(^\circ)$	$\tau(^\circ)$	$du^c/m^c(\mu m)$	$dv^c/m^c(\mu m)$	(u_0^c, v_0^c)	k^c
Value	353.347	13.786	15.017	15.017	(964, 724)	−18.113
Parametre	$\alpha^c(^\circ)$	$\beta^c(^\circ)$	$\gamma^c(^\circ)$	$t_x^c(m)$	$t_y^c(m)$	
Value	22.070	359.889	181.252	−0.00024	0.000862	

$$T_{3\times3}=\begin{bmatrix} Q_{2\times2} & 0 \\ 0 & 1 \end{bmatrix}^{-1} \tag{5}$$

In Eq. (5),

$$Q_{2\times2}=\begin{bmatrix} (\cos\rho)^2(1-\cos\tau)+\cos\tau & \cos\rho\sin\rho(1-\cos\tau) \\ \cos\rho\sin\rho(1-\cos\tau) & (\sin\rho)^2(1-\cos\tau)+\cos\tau \end{bmatrix} \tag{6}$$

where τ is the angle between the optical axis and perpendicular line⊥of CCD chip plane, with $0^\circ < \tau < 90^\circ$, and ρ is the angle between the projection on CCD chip plane of optical axis and v axis of CCD chip plane, $0^\circ \le \rho \le 360^\circ$, as shown in Fig. 9.

m^c is the magnification of the bilateral telecentric lens. du^c and dv^c are the horizontal and vertical sizes, respectively, of the camera pixels. During calibration, either du^c/m^c or dv^c/m^c is regarded

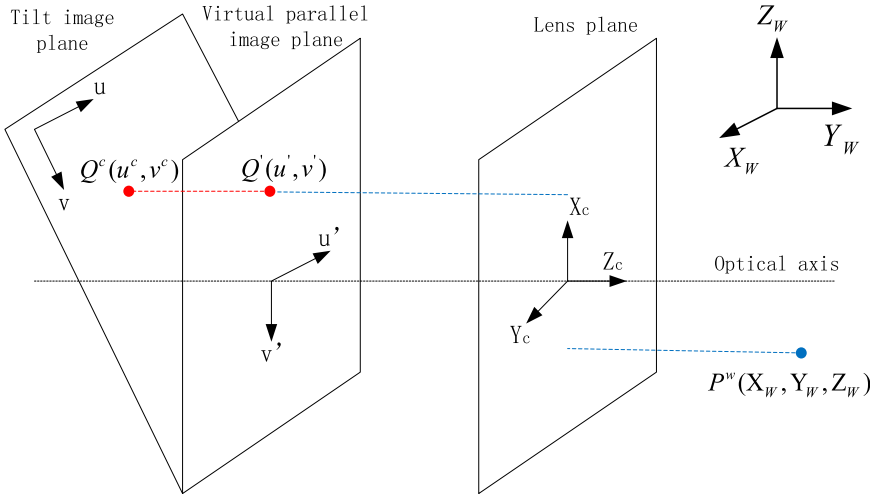

Fig. 8. Imaging model of telecentric camera on Scheimpflug condition.

Table 2
The inner and external parametres of telecentric projector.

du^p/m^p(μm)	dv^p/m^p(μm)	$(u_0^p v_0^p)$	k^p	$\alpha^p(^\circ)$	$\beta^p(^\circ)$	$\gamma^p(^\circ)$	t_x^p(m)	t_y^p(m)
30.535	15.335	(320, 400)	−36.799	351.542	357.865	2.402	0.000987	0.000477

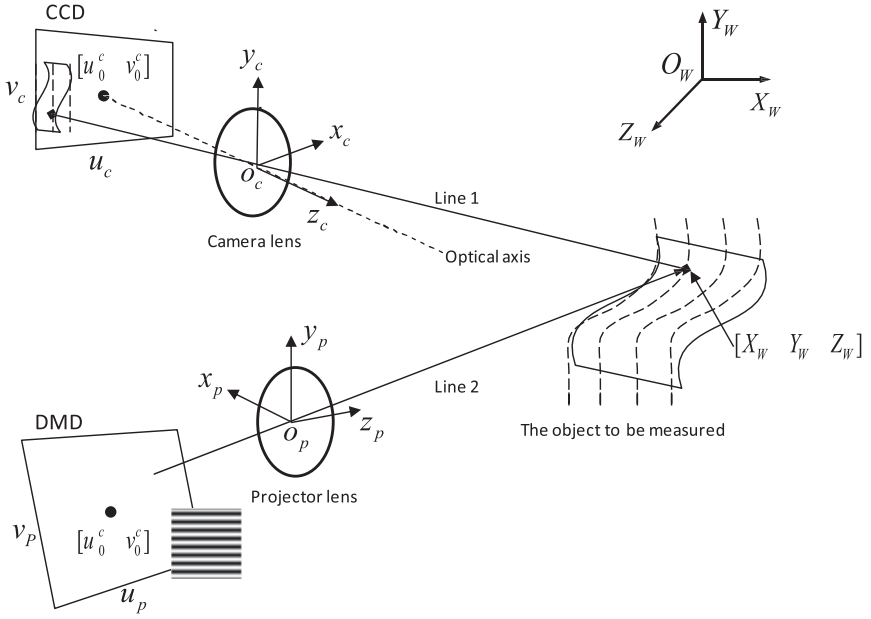

Fig. 10. Schematic diagram of 3D reconstruction principle.

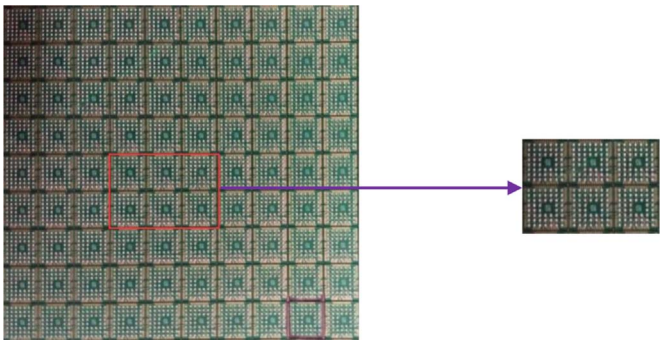

Fig. 11. The wafer to be measured.

as entirety, denoting the horizontal and vertical sizes, respectively, of the camera pixel that is converted into the WCS. $(u_0^c v_0^c)$ is the center point coordinate of the CCD chip. r_{ij} are the elements of the rotation matrix R^c, and t_x^c and t_y^c are the elements of the translation matrix.

To obtain a more accurate measurement result, it is necessary to consider the distortion, although that of the telecentric lens is very low. When the division model is used, the distorted coordinates can be transformed from undistorted coordinates by the following equations:

$$\widetilde{u}'=\frac{2u'}{1+\sqrt{1-4k^c\left(u'^2+v'^2\right)}} \text{ and } \widetilde{v}'=\frac{2v'}{1+\sqrt{1-4k^c\left(u'^2+v'^2\right)}} \tag{7}$$

A ceramic plate with a precise planar circle pattern is employed for the calibration. The ceramic plate is arbitrarily put in dozens of poses, whose images are captured by the camera. Then, through the calibration algorithm of the telecentric camera in the Scheimpflug condition in Halcon 12.0, the inner and external parametres of the camera (relative to one pose of the ceramic plate, i.e., WCS) can be obtained, as shown in Table 1. The inner parametres include ρ, τ, du^c/m^c, dv^c/m^c, $(u_0^c v_0^c)$, and the distortion k^c, and the external parametres include the rotation angles α^c, β^c, γ^c of the x, y, z axes, which constitute the rotation matrix R^c, and the translation component t_x^c, t_y^c.

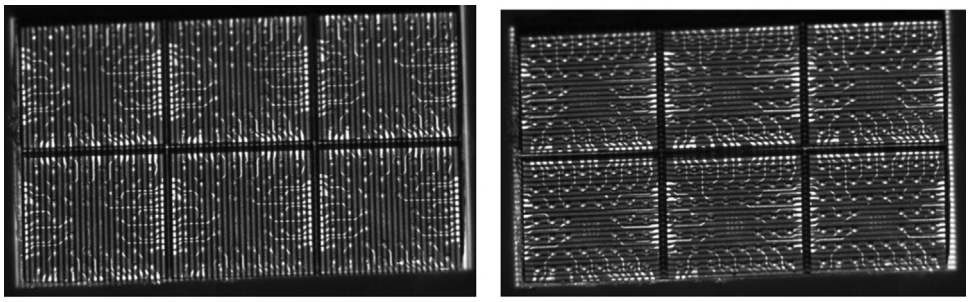

(a) (b)

Fig. 12. The wafer covered by fringe pattern on measuring. (a) Covered by vertical fringe. (b) Covered by horizontal fringe.

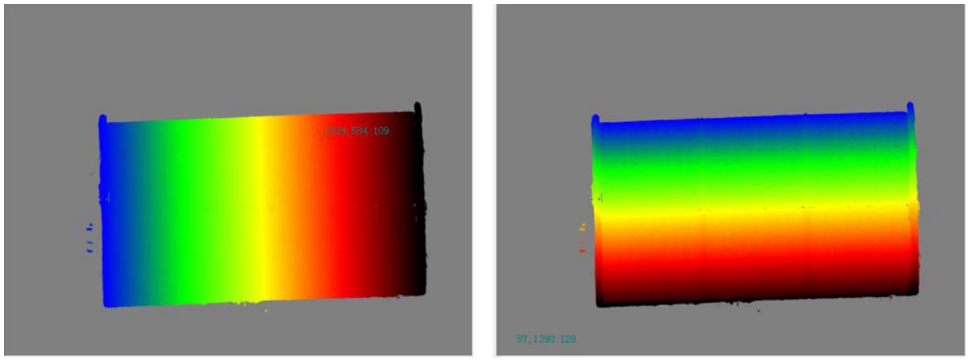

(a) (b)

Fig. 13. Phase maps for fringe images. (a) For vertical fringe images. (b) For Horizontal fringe images.

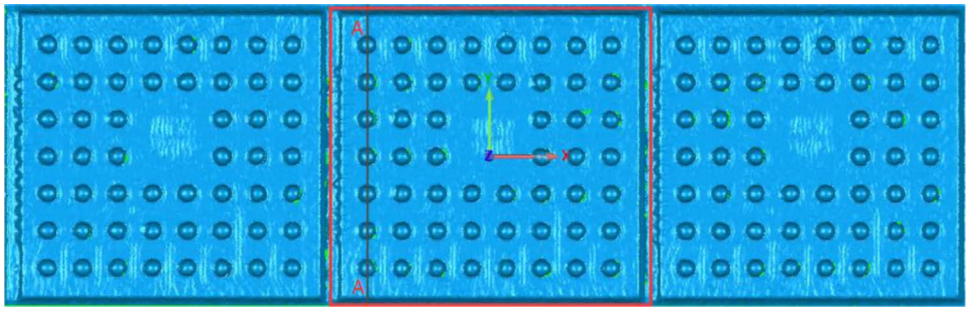

Fig. 14. The 3D model of the wafer.

3.2. Calibration of telecentric projector

A series of horizontal and vertical fringe patterns as the phase carrier is projected onto the ceramic plate, which is put arbitrarily in dozens of poses, and the camera captures the images. Although the telecentric projector is unable to capture images, through the method of phase matching, the camera images can be converted into projector images; thus, the telecentric projector can be calibrated as a reverse telecentric camera. The mapping relation between the pixels on the CCD of the camera and the DMD of the DLP projector can be written as

$$u^p=\frac{\Phi_v(u^c, v^c)}{N_v\times 2\pi}\times W \tag{8}$$

$$v^p=\frac{\Phi_h(u^c, v^c)}{N_h\times 2\pi}\times H \tag{9}$$

where (u^p, v^p) is the pixel point on the DMD of the DLP projector; (u^c, v^c) is the pixel point on the CCD of camera; and $\Phi_v(u^c, v^c)$ and $\Phi_h(u^c, v^c)$ are the absolute phases of the pixel point (u^c, v^c) on the vertical and horizontal fringe images, respectively, which can be solved by the aforementioned gray code-combined phase-shift algorithm. N_v and N_h are the period numbers of the vertical and horizontal fringe images, respectively. W and H are the horizontal and vertical resolutions, respectively, of the projector.

According to the telecentric camera imaging model, the mapping equation from point $P^w(X_w, Y_w, Z_w)$ in WCS to the pixel point $Q^p(u^p, v^p)$ in the PCS of the projector can be written as

$$\begin{bmatrix} u^p \\ v^p \\ 1 \end{bmatrix}=\begin{bmatrix} m^p/du^p & 0 & u_0^p \\ 0 & m^p/dv^p & v_0^p \\ 0 & 0 & 1 \end{bmatrix}\begin{bmatrix} r_{11} & r_{12} & r_{13} & t_x^p \\ r_{21} & r_{22} & r_{23} & t_y^p \\ 0 & 0 & 0 & 1 \end{bmatrix}\begin{bmatrix} X_w \\ Y_w \\ Z_w \\ 1 \end{bmatrix} \tag{10}$$

where m^p is the magnification of object telecentric lens, and du^p and dv^p are the horizontal and vertical sizes of the projector pixel, respectively. During calibration, either du^p/m^p or dv^p/m^p is regarded as entirety, which denote the horizontal and vertical sizes, respectively, of the projector pixel that is converted to the WCS. (u_0^p, v_0^p) is the center point coordinate of the DMD chip. r_{ij} are the elements of the rotation matrix, and R^p, t_x^p, and t_y^p are the elements of the translation matrix.

As with calibrating a camera, the lens distortion must be considered, which herein is denoted by k^p. Similarly, using the calibration algorithm of telecentric camera in Halcon 12.0, the inner and external parametres (relative to the same WCS with the camera) of the telecentric projector can be obtained, as shown in Table 2. The inner parametres include du^p/m^p, dv^p/m^p, (u_0^p, v_0^p), and the distortion k^p, and the external parametres include the rotation angles α^p, β^p, γ^p of the x, y, z, which constitute the rotation matrix R^p, and the translation components t_x^p, t_y^p.

3.3. Relative pose between camera and projector

From Sections 3.1 and 3.2, the external parametres of the camera and projector relative to the same WCS (bound on one pose of the ceramic plate) are obtained, which is expressed by the following equations:

$$P^c=M^cP^w \text{and } P^p=M^pP^w \tag{11}$$

where $P^c=\{x^c, y^c, z^c\}^T$, $P^p=\{x^p, y^p, z^p\}^T$, $P^w=\{x^w, y^w, z^w\}^T$ are the coordinates of the point P in the camera coordinate system, projector coordinate system, and world coordinate system, respectively, and $M^c=[R^c, t^c]$ and $M^p=[R^p, t^p]$ are the conversion relationships from the camera and projector coordinate system, respectively, to the WCS. Using Eq. (11), it is easy to determine the relative pose M between the camera and projector:

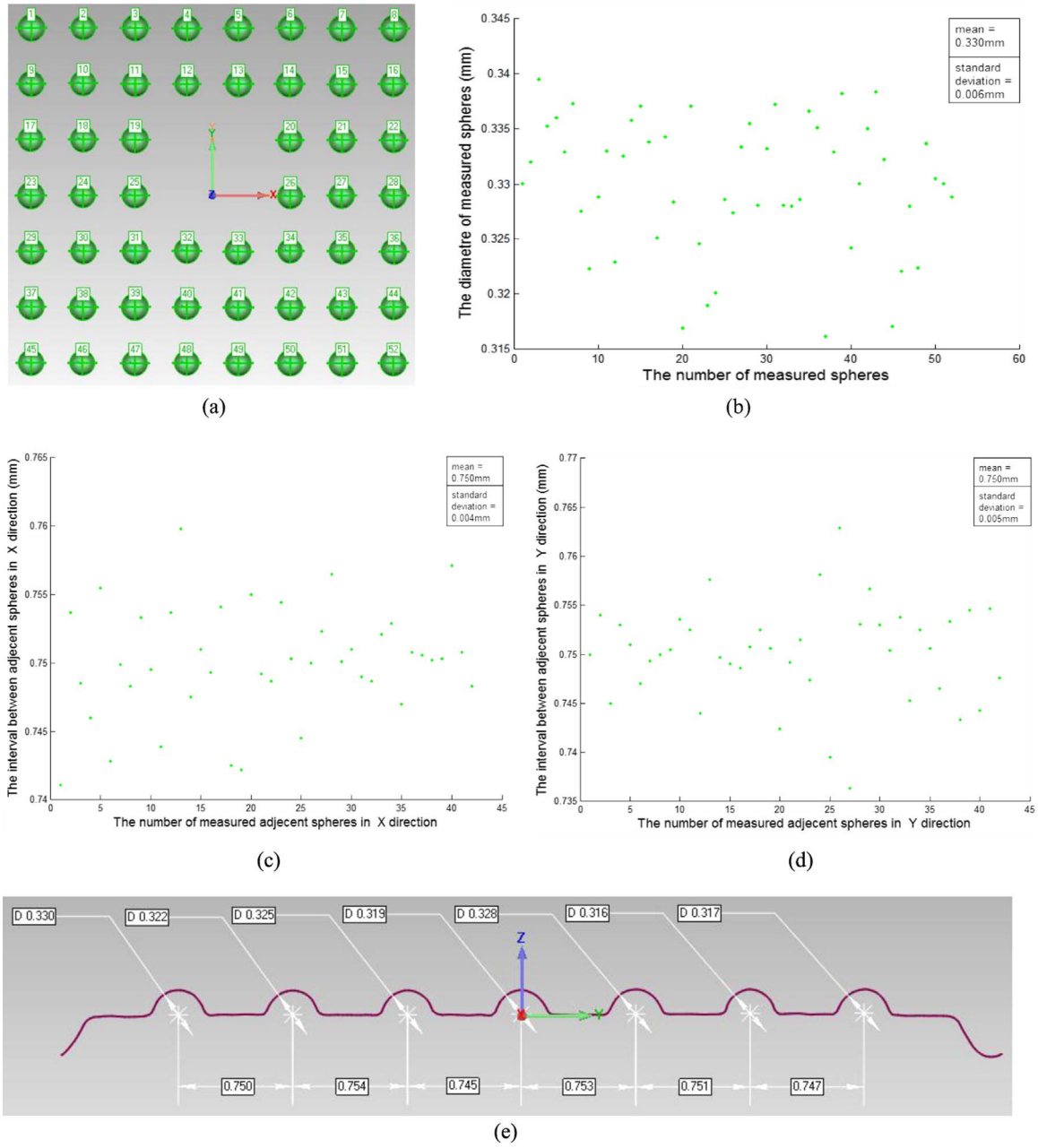

Fig. 15. The dimensional measurement of one piece of wafer unit. (a) One piece of wafer unit. (b) The diameter of spheres. (c) The interval between adjacent spheres in X direction. (d) The interval between adjacent spheres in Y direction. (e) The sectional view taken along line A – A of Fig.14.

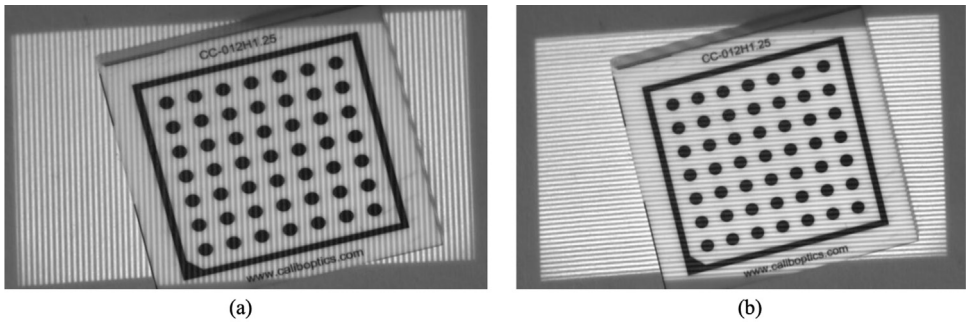

Fig. 16. The ceramic plate image combined with WCS. (a) Covered by vertical fringe. (b) Covered by horizontal fringe.

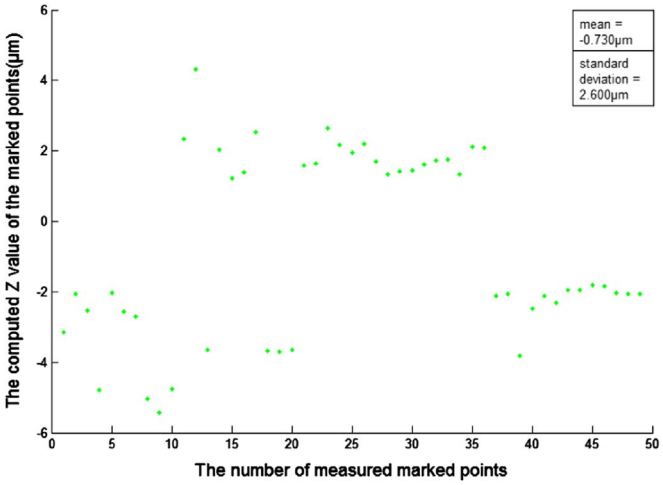

Fig. 17. The computed z value of the marked points.

$$M = M^c[M^p]^{-1} = \begin{bmatrix} -0.9990 & -0.0256 & -0.0359 & 0.0369 \\ 0.0333 & -0.9716 & -0.2344 & 0.2373 \\ -0.0289 & -0.2354 & 0.9715 & -0.9778 \end{bmatrix} \quad (12)$$

While implementing the computation, the homogeneous coordinates $P^w=\{x^w, y^w, z^w,1\}^T$ are employed; thus, the matrix M has four columns.

4. 3D reconstruction

According to the telecentric camera imaging model on Scheimpflug condition, the mapping equation from point $P^w(X_w, Y_w, Z_w)$ in the WCS to the pixel point $Q^c(u^c, v^c)$ in the PCS of the camera, i.e., the equation of line 1 in Fig. 9, can be written as

$$[u^c \quad v^c \quad 1]^T = T_{3\times3}A^cM^c[X_w \quad Y_wZ_w \quad 1]^T \quad (13)$$

Similarly, according to the telecentric camera imaging model, the mapping equation from the point $P^w(X_w, Y_w, Z_w)$ in the WCS to the pixel point $Q^p(u^p, v^p)$ in the PCS of the projector, i.e., the equation of line 2 in Fig. 9, can be written as

$$[u^p \quad v^p \quad 1]^T = A^pM^p[X_w \quad Y_wZ_w \quad 1]^T \quad (14)$$

The mapping relation between the pixel on the CCD of the camera and the DMD of the DLP projector can be expressed by Eqs. (8) and (9).

By solving Eqs. (8), (9), (13), and (14), the point $P^w(X_w, Y_w, Z_w)$ in space can be obtained, as shown in Fig. 10. Via a third-party point cloud processing software, we can obtain the 3D model of the object to be measured.

5. Experiment and discussion

As shown in Fig. 11, an experiment on the 3D reconstruction of the wafer surface is implemented. The depth of focus of the camera lens is 6 mm, which represents the measurement range in the Z direction. The dimensions of one piece of the wafer unit are approximately 6.5 mm × 6.5 mm; thus, the measurement system, whose measurement range is 20 mm × 13 mm × 6 mm, can cover 6 (2 × 3) pieces of the wafer unit. As shown in Fig. 12, a series of vertical and horizontal fringe patterns is projected onto the wafer, which are captured by the camera meanwhile. Then, the phase unwrapping for the fringe images is performed, and the absolute phases—increasing from blue to red—are obtained, as shown in Fig. 13. Finally, the 3D model of the wafer is obtained, as shown in Fig. 14. Unfortunately, only the half-wafer 3D model is reconstructed well, owing to the shinning problem and the bad focusing problem caused by the installation problem of the projector lens for the other half. If we install the projector lens precisely and solve the shinning problem, we will gain a better 3D model of the wafer.

As shown in Fig. 14, the obtained 3D model of the wafer is imported into the 3D metrology software Geomagic Quilify, and the middle wafer unit is selected to accomplish the dimensional measurement of the spheres on the wafer, whose CAD model is obtained by the best fitting method, as shown in Fig. 15(a). One piece of the wafer unit contains 52 spheres, with a nominal diameter of 0.33 mm and an interval between adjacent spheres of 0.75 mm. Fig. 15(b) shows the diameter of the measured 52 spheres, whose mean is 0.330 mm and standard deviation is 0.006 mm. The intervals between adjacent spheres in the X direction are shown in Fig. 15(c), with a mean of 0.750 mm and deviation of 0.004 mm. The intervals between adjacent spheres in the Y direction are shown in Fig. 15(d), with a mean of 0.750 mm and deviation of 0.005 mm. To be more clear, a sectional view is taken along the line A–A of Fig. 14, and the diameter and intervals of the spheres are marked as shown in Fig. 15(e). In Figs. 14 and 15 (a)–(e), it is clear that the designed measurement system can well reconstruct the 3D model of the wafer and that both the measured diameter and interval of the spheres are close to the nominal values.

The resolution of the camera lens is 20 μm, which represents the lateral resolution of the measurement system. Theoretically, the vertical resolution of the measurement system can reach 2 μm. To evaluate the practical vertical resolution of the measurement system, as shown in Fig. 16, we select a ceramic plate image with which the is WCS combined, solve the coordinates in the WCS of the marked points, and compare the computed Z values with the theoretical values. The theoretical values constantly equal 0. The computed Z values are shown in Fig. 17. The mean value is −0.730 μm, and the standard deviation is 2.600 μm, which is close to the theoretical vertical resolution of 2 μm.

6. Conclusion

We designed a new 3D measuring system for micro components: a structure light telecentric stereoscopic vision 3D measurement system based on the Scheimpflug condition. By replacing the projector lens and camera lens with an object-side telecentric lens and bilateral telecentric lens with Scheimpflug adjustments, respectively, the proposed system creatively combines the telecentric imaging model and Scheimpflug condition on the basis of structure light stereoscopic vision. In the Scheimpflug condition, the depth of focus can be enlarged greatly without decreasing the lens resolution, which ensures that the measurement system has a good resolution over a wide measurement range. The system measurement range is 20 mm × 13 mm × 6 mm, the lateral resolution is 20 μm, and the practical vertical resolution reaches 2.6 μm, which is close to the theoretical vertical resolution of 2 μm. This brings the benefits of a wide measurement range, high accuracy, fast speed, and low price, which well satisfies the 3D measurement needs of micro components such as semiconductor devices, photoelectron elements, and MEMS. Unfortunately, only the half-wafer 3D model is reconstructed well, owing to the shinning problem and the bad focusing problem caused by the installation problem of the projector lens for the other half. If we install the projector lens precisely and solve the shinning problem, we will obtain a better 3D model of the wafer.

Acknowledgments

This work was supported by the National Basic Research Program of China (973 Program No. 2011CB013104), the Guangdong Provincial Natural Science Foundation (No. 2015A030312008, 2016A030308016) and the R&D Key Projects from Guangdong Province (No. 2015B010104008, No. 2015B010133005).

Appendix A. Supplementary material

Supplementary data associated with this article can be found in the online version at http://dx.doi.org/10.1016/j.optlaseng.2016.05.021.

References

[1] Dai Gaoliang, Butefisch Sebastian, Pohlenz Frank, Danzebrink Hans-Ulrich. A high precis-ion micro/nano CMM using piezoresistive tactile probes. Meas Sci Technol 2009;20:084001.
[2] Claverley JD, Leach RK. A review of the existing performance verification infrastructure for micro-CMMs. Precis Eng 2015;39:1–15.
[3] Hung Chuan-Cheng, Fang Yi-Chin, Tsai Cheng-Mu, Lin Chang-Ching, et al. Optical design of high performance con-focal microscopy with digital micromirror and stray light filters. Optik 2010;121:2073–9.
[4] Apedo KL, Munzer C, He H, Montgomery P, Serres N, Fond C, Feugeas F. Cement paste surface roughness analysis using coherence scanning interferometry and confocal microscopy. Mater Charact 2015;100:108–19.
[5] Kumar U Paul, Bhaduri Basanta, Kothiyal MP, Mohan N Krishna. Two-wavelength micro-interferometry for 3-D surface profiling. Opt Lasers Eng 2009;47:223–9.
[6] Kumar U Paul, Haifeng Wang, Krishna Mohan N, Kothiyal MP. White light interferometry for surface profiling with a colour CCD. Opt Lasers Eng 2012;50:1084–8.
[7] Windecker Robert, Franz Stefan, Tiziani Hans J. Optical roughness measurements with fringe projection. Appl Opt 1999;38(13):2837–42.
[8] Zhang C, Huang PS, Chiang FP. Microscopic phase-shifting profilometry based on digital micromirror device technology. Appl Opt 2002;41(28):5896–904.
[9] Li Ameng, Peng Xiang, Yin Yongkai, et al. Fringe projection based quantitative 3D microscopy. Optik 2013;124:5052–6.
[10] Yin Y, Wang M, Gao BZ, Liu X, Peng X. Fringe projection 3D microscopy with the general imaging model. Opt Express 2015;23:6846–57.
[11] ⟨http://www.opto-e.cn/resources/telecentric-lenses-tutorial⟩; [accessed on 05.04.15].
[12] ⟨https://en.wikipedia.org/wiki/Orthographic_projection⟩; [accessed on 06.04.15].
[13] Li Dong, Tian Jindong. An accurate calibration method for a camera with telecentric lenses. Opt Lasers Eng 2013;51:538–41.
[14] Li Dong, Liu Chunyang, Tian Jindong. Telecentric 3D profilometry based on phase shifting fringe projection. Opt Express 2014;22(26):31826–35.
[15] Frankowski G, Hainich R. Network Based Multi-Sensor Optical 3D Acquisition of Complex Structures. Proc SPIE 2012;8254:1–10.
[16] ⟨https://en.wikipedia.org/wiki/Scheimpflug_principle⟩; [accessed on 26.04.15].
[17] Peng Junzheng, Peng Xiang, et al. Distortion correction for microscopic fringe projection system with Scheimpflug telecentric lens. Appl Opt 2015;54 (34):10055–62.
[18] ⟨https://www.opto-e.cn/products/tcsm-model-TCSM036⟩; [accessed on 06.05.15].
[19] Jiang X, Bunke H. Range data acquisition by coded structured light: error characteristic of binary and gray projection code. Proc SPIE 1994;2252.